Journal of Computational Physics 305 (2016) 521–538

Contents lists available at ScienceDirect

Journal of Computational Physics

www.elsevier.com/locate/jcp

Adaptive Haar wavelets for the angular discretisation of spectral wave models

Alexandros Adam [a,*], Andrew G. Buchan [a], Matthew D. Piggott [a], Christopher C. Pain [a], Jon Hill [b], Mark A. Goffin [a]

[a] Applied Modelling and Computation Group, Department of Earth Science and Engineering, Imperial College London, SW7 2AZ, UK
[b] Environment Department, University of York, Heslington, York YO10 5DD, UK

ARTICLE INFO

Article history:
Received 29 May 2015
Received in revised form 25 October 2015
Accepted 26 October 2015
Available online 2 November 2015

Keywords:
Spectral wave modelling
Action balance equation
Adaptivity
Angular adaptivity
Haar wavelets

ABSTRACT

A new framework for applying anisotropic angular adaptivity in spectral wave modelling is presented. The angular dimension of the action balance equation is discretised with the use of Haar wavelets, hierarchical piecewise-constant basis functions with compact support, and an adaptive methodology for anisotropically adjusting the resolution of the angular mesh is proposed. This work allows a reduction of computational effort in spectral wave modelling, through a reduction in the degrees of freedom required for a given accuracy, with an automated procedure and minimal cost.

1. Introduction

A wide range of different numerical models are now available which can be used for the study of wave generation and propagation. These can be split into two main categories: phase-resolving and phase-averaging [1]. Phase-resolving models, such as potential flow, mild-slope, Boussinesq and full 3D Navier–Stokes models represent the sea surface elevation in space and time and accurately account for the non-linear processes. They are, however, computationally expensive and, thus, restricted to relatively small scale applications. Phase-averaging models are based on a spectral description of the waves and though the non-linearities are represented by parametrised formulations, they are cheap enough to be used on larger problem domains.

Spectral wave modelling first appeared after the introduction of the wave energy spectrum by Pierson [2] and the introduction of the energy balance equation by Gelci [3]. Based on linear wave theory, the sea surface elevation is composed of a superposition of harmonic wave components and the energy spectrum $E(x, y, f, \theta, t)$ represents the energy content over frequencies f and directions θ, in space (x, y) and time t. All of the important characteristics of the sea surface, such as the significant wave height or the mean period, can then be seen as statistical parameters of the spectrum and derived from various combinations of its moments $m_n = \int\int f^n E(f, \theta) df d\theta$ [4].

The energy spectrum is calculated based on the conservation of energy in an Eulerian framework. A kinematic part representing the propagation of wave energy is balanced with a set of source terms which represent wind generation, non-linear energy transfers and wave dissipation. Various spectral wave models have been developed from as early as the

* Corresponding author.
E-mail address: a.adam12@imperial.ac.uk (A. Adam).

http://dx.doi.org/10.1016/j.jcp.2015.10.046

1960s. So-called "first-generation models" did not account (or loosely accounted) for non-linear wave energy interactions. "Second-generation" models used a simplified parametrised form for these interactions, restricting the shape of the spectrum. A thorough review of these early models can be found in [5].

The next milestone in spectral wave modelling came from the WAMDI group [6] with the introduction of WAM, a model with improved formulations for the source terms and no a-priori restriction on the shape of the spectrum. This framework was coined as "third-generation" wave modelling and followed by rapid developments. Currents were included in the formulation by rewriting the governing equation in terms of the action density $A = E/f$, which is conserved in a relative frame of reference moving with the current [7]. The action balance equation was then extended to account for shallow water propagation, such as shoaling and refraction and shallow water non-linear processes, such as triads and depth induced breaking. For a thorough review of the most notable developments the reader can refer to [8] and [9]. Today the most widely used third generation models by the community are WAM [6] and WAVEWATCHIII [10] for global scales and SWAN [11] for coastal applications.

The source parameterisations and the numerical schemes for spectral wave models are still an active field of research. The last five years, for example, has seen the error levels for the prediction of significant wave heights and mean periods in the middle of the ocean drop by 20% and 30% respectively [12]. A further reduction in these errors necessitates an increase in computational resolution, to resolve coastal processes while still covering large domains [13]. An important step towards this direction has been the use of unstructured meshes for the spatial discretisation [14–17].

In the ocean circulation modelling community, the wide range of spatial and temporal scales has motivated the development of spatially adaptive schemes, as a means of local and anisotropic dynamical mesh refinement. Various techniques have been developed, with examples including the structured tree-based hierarchical finite volume Gerris [18] model and the unstructured finite element Fluidity [19] model. The first effort to apply these techniques to the energy balance equation was made by Popinet et al. [20] who combined the adaptive solver of Gerris with WAVEWATCHIII to develop a spatially adaptive spectral wave model. In their work they showed a decrease of one to two orders of magnitude in run-times for practical spatial resolutions. More recently Meixner [21] was the first to apply adaptivity in phase space. By developing a discontinuous finite element spectral wave model, p-adaptivity was applied both in geographic and spectral space. Adjusting the order of the finite element expansions gave significant speed-ups compared to using uniform higher order expansions, in a deep water propagation test case.

This work focuses on applying adaptivity for the refinement of the angular resolution. It is not easy to quantify the directional distribution of ocean waves in a general framework. Observations, however, show that the directional distribution tends to be sharp around the peak frequency [22,23]. As waves propagate outside of their generation area, direction-dispersion further enhances this. Thus, in many cases the energy spectrum only contains energy in a narrow band of directions. (This is even more obvious in coastal areas where waves appear to come from a single direction.) Viewed in this perspective, uniform angular resolutions in spectral wave models are inefficient since for a specific point not all angles have non-zero energy. The adaptive approach proposed here attempts to deal with this problem though the use of compactly supported wavelet basis functions. These can locally resolve details in the angular dimension resulting in a different angular mesh for each computational point.

Wavelets, became an active field of research in the 1980s, with the works of researchers such as Morlet, Grossman and Daubechies [24] on signal processing. Starting as an alternative to Fourier analysis, their popularity soon expanded, owing mainly to the localised nature of wavelet basis in frequency and time, as well as their hierarchical structure. This meant that a localised wavelet transform could be performed with a variable-resolution reconstruction of a signal, which is ideal for applications such as data and image compression [25–27]. These advantages soon drew the attention of the numerical modelling community, as the aforementioned properties provided an efficient framework for adaptive algorithms. Since then, wavelets have been applied to various fields of numerical analysis, including turbulence modelling [28] and partial differential equations such as the Navier–Stokes [29,30], hyperbolic [31,32] and parabolic systems [33,34]. A more comprehensive list of wavelets used in PDE's can be found in [35].

Of more relevance to this work, is the use of wavelets for the discretisation of the Boltzmann transport equation, which provides a natural framework for spectral wave modelling. Both the Boltzmann transport (in non-scattering media) and the energy balance equations are multi-dimensional hyperbolic systems, dealing with the propagation of an energy flux in geographic and phase space [36]. It is worth noting that the energy balance equation is also known as the radiative transfer equation. In the case where only four-wave interactions are considered for the source terms it is also known as the Boltzmann equation [37, p. 30]. Buchan et al. [38] first applied linear and quadratic wavelets for resolving the angular dependence of the Boltzmann transport equation, and then went on to show how they can be used for the application of angular adaptivity [39]. Goffin et al. [40] then extended this to apply goal-based measures to the error metrics driving adaptivity.

In this paper Haar wavelets (named after Alfred Haar) – piecewise constant, hierarchical, compactly supported basis functions – are used for the angular discretisation of the action balance equation and the application of anisotropic angular adaptivity. Haar wavelets are chosen for their simplicity, as well as the fact that they produce sparse system matrices compared to higher order wavelet expansions. For a historical background and an overview of wavelets in general and Haar wavelets in particular the reader can refer to [41], while a more rigorous mathematical background and review of their numerical applications can be found in [42].

The paper is organised as follows. First in Section 2 the action balance equation and its discretisation is presented. Then in Section 3 a brief theoretical background of wavelets is given and the Haar wavelet functions are introduced. This is then followed by the development of the adaptive framework and the description of the adaptive algorithm in Section 4. Finally in Section 5 angular adaptivity is applied on both stationary and time-dependent test cases and the benefits of the scheme are quantified, in terms of the required degrees of freedom as well as computational run-times. The paper concludes with a general overview of the results.

2. Action balance equation

2.1. Introduction

The action balance equation in Cartesian coordinates can be written as [4]

$$\frac{\partial N}{\partial t}+\frac{\partial (c_{g_x}+u_x)N}{\partial x}+\frac{\partial (c_{g_y}+u_y)N}{\partial y}+\frac{\partial c_\sigma N}{\partial \sigma}+\frac{\partial c_\theta N}{\partial \theta}=\frac{S_{\text{tot}}}{\sigma}, \tag{1}$$

where the action density spectrum $N(\mathbf{r},\theta,\sigma,t)\,(\mathrm{J\,m^{-2}\,rad^{-3}\,s^2})$ is dependent on geographical space $\mathbf{r}=(x,y)\,(\mathrm{m})$, spectral space (θ,σ), i.e. direction of travel $\theta\,(\mathrm{rad})$ and relative frequency $\sigma=2\pi f\,(\mathrm{rad\,s^{-1}})$, the frequency in a frame of reference moving with the current, and time $t\,(\mathrm{s})$. Here $S_{\text{tot}}\,(\mathrm{J\,m^{-2}\,rad^{-2}\,s})$ are the source terms, $\mathbf{c_g}=(c_{g_x},c_{g_y})=\big(c_g\cos(\theta),c_g\sin(\theta)\big)\,(\mathrm{m\,s^{-1}})$ is the group velocity, $\mathbf{u}=(u_x,u_y)\,(\mathrm{m\,s^{-1}})$ is the current velocity and $c_\sigma\,(\mathrm{rad\,s^{-2}})$, $c_\theta\,(\mathrm{rad\,s^{-1}})$, are the propagation speeds in the frequency and angle dimension respectively. These propagation speeds are

$$c_g=\frac{1}{2}\Big(1+\frac{2kd}{\sinh(2kd)}\Big)\sqrt{\frac{g\tanh(kd)}{k}}, \tag{2}$$

$$c_\sigma=\frac{d\sigma}{dt}=\frac{\partial\sigma}{\partial d}\Big[\frac{\partial d}{\partial t}+\mathbf{u}\cdot\nabla d\Big]-c_g\mathbf{k}\cdot\frac{\partial\mathbf{u}}{\partial s}, \tag{3}$$

$$c_\theta=\frac{d\theta}{dt}=-\frac{1}{k}\Big[\frac{\partial\sigma}{\partial d}\frac{\partial d}{\partial m}+\mathbf{k}\cdot\frac{\partial\mathbf{u}}{\partial m}\Big], \tag{4}$$

where $k=2\pi/L\,(\mathrm{rad\,m^{-1}})$ is the wavenumber and $\mathbf{k}=\big(k\cos(\theta),k\sin(\theta)\big)$ the wavenumber vector, $L\,(\mathrm{m})$ is the wavelength, $d\,(\mathrm{m})$ the bathymetric value, $g\,(\mathrm{m\,s^{-2}})$ the acceleration due to gravity, and $s\,(\mathrm{m})$ is a coordinate in the direction of propagation $\hat{s}=\big(\cos(\theta),\sin(\theta)\big)$, while $m\,(\mathrm{m})$ is a coordinate perpendicular to the direction of propagation $\hat{m}=\big(-\sin(\theta),\cos(\theta)\big)$. To evaluate these expressions the value of the wavenumber is needed, which can be calculated from the dispersion relationship in a relative frame of reference, i.e. a frame of reference moving with the current,

$$\sigma^2=gk\tanh(kd). \tag{5}$$

2.2. Angular discretisation

In this work, for simplicity, wave-current interactions and source terms are neglected. Omitting these, the action balance equation becomes

$$\frac{\partial N(\mathbf{r},t,\theta)}{\partial t}+\nabla\cdot\Big(\mathbf{c_g}(\mathbf{r},t,\theta)N(\mathbf{r},t,\theta)\Big)+\frac{\partial\big(c_\theta(\mathbf{r},t,\theta)N(\mathbf{r},t,\theta)\big)}{\partial\theta}=0. \tag{6}$$

A finite element expansion is used for the representation of the angular dimension. An arbitrary angular discretisation is considered, in which θ is represented by the span of angular trial functions G_j, $j\in\{1,2,\ldots,K\}$, such that

$$N(\mathbf{r},t,\theta)\approx\sum_{j=1}^{K}N_j(\mathbf{r},t)G_j(\theta). \tag{7}$$

To derive the weak formulation of the problem a set of test functions is required. For this work the Galerkin method is used [43], in which the trial and test functions are the same. Weighting the action balance equation with the set of test functions G_i, $i\in\{1,2,\ldots,K\}$, gives

$$\begin{aligned}\int_\theta G_i(\theta)\frac{\partial N(\mathbf{r},t,\theta)}{\partial t}d\theta+\int_\theta G_i(\theta)\nabla\cdot\Big(\mathbf{c_g}(\mathbf{r},t,\theta)N(\mathbf{r},t,\theta)\Big)d\theta+\\ \int_\theta G_i(\theta)\frac{\partial c_\theta(\mathbf{r},t,\theta)N(\mathbf{r},t,\theta)}{\partial\theta}d\theta=0,\quad\forall\, i\in\{1,2,\ldots,K\},\end{aligned} \tag{8}$$

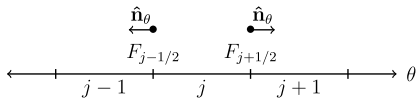

Fig. 1. Example of an element j of the angular dimension θ, the angular flux $F_{j\pm1/2}$ and the normals $\hat{\mathbf{n}}_\theta$ at the element boundaries.

where θ is the one-dimensional angular coordinate. For the last term of (8), applying the divergence theorem gives

$$\int_\theta G_i(\theta)\frac{\partial c_\theta(\mathbf{r},t,\theta)N(\mathbf{r},t,\theta)}{\partial\theta}d\theta = \int_S G_i(\theta)c_\theta(\mathbf{r},t,\theta)N(\mathbf{r},t,\theta)\hat{\mathbf{n}}_\theta dS - \int_\theta \frac{dG_i(\theta)}{d\theta}c_\theta(\mathbf{r},t,\theta)N(\mathbf{r},t,\theta)d\theta, \quad \forall\, i\in\{1,2,\ldots,K\}, \tag{9}$$

where S corresponds to the boundary surface and $\hat{\mathbf{n}}_\theta$ to the outward normal unit vector. Given that the domain θ is one-dimensional S reduces to a point and $\hat{\mathbf{n}}_\theta$ is 1 and -1 on the two boundary nodes of each angular element respectively (Fig. 1).

A first-order upwind scheme is applied to resolve the angular inter-element boundary conditions. This is used to ensure the successful implementation of the numerical schemes, due to its simplicity and numerical stability, before higher order approximations are applied (such as the QUICKEST scheme [44]). For a specific angular element j the flux $F = c_\theta N$ from the two boundaries at $j-\frac{1}{2}$ and $j+\frac{1}{2}$ (Fig. 1) is

$$\begin{aligned}
&F_{j-\frac{1}{2}} = c_{\theta\, j-\frac{1}{2}}N_{j-\frac{1}{2}}; && && F_{j+\frac{1}{2}} = c_{\theta\, j+\frac{1}{2}}N_{j+\frac{1}{2}}, && \\
&c_{\theta\, j-\frac{1}{2}} = 0.5\left(c_{\theta\, j-1}+c_{\theta\, j}\right); && && c_{\theta\, j+\frac{1}{2}} = 0.5\left(c_{\theta\, j}+c_{\theta\, j+1}\right), && \\
&N_{j-\frac{1}{2}} = N_{j-1} && c_\theta \geq 0; && N_{j+\frac{1}{2}} = N_j && c_\theta \geq 0, \\
&N_{j-\frac{1}{2}} = N_j && c_\theta < 0; && N_{j+\frac{1}{2}} = N_{j+1} && c_\theta < 0.
\end{aligned} \tag{10}$$

Formulating the whole system in vector form gives

$$\mathbf{M}\frac{\partial\mathbf{N}(\mathbf{r},t)}{\partial t} + \Big(\mathbf{A}c_g(\mathbf{r},t)\Big)\cdot\nabla\mathbf{N}(\mathbf{r},t) + \nabla\cdot\Big(\mathbf{A}c_g(\mathbf{r},t)\Big)\mathbf{N}(\mathbf{r},t) + \mathbf{H}_\theta(\mathbf{r},t)\mathbf{N}(\mathbf{r},t) = 0, \tag{11}$$

where

$$\mathbf{A} = (\mathbf{A_x},\mathbf{A_y}), \tag{12}$$

$$\mathbf{A_x} = \sum_{j=1}^{K}\int_\theta G_i(\theta)\cos(\theta)G_j(\theta)d\theta, \quad \forall\, i\in\{1,2,\ldots,K\}, \tag{13}$$

$$\mathbf{A_y} = \sum_{j=1}^{K}\int_\theta G_i(\theta)\sin(\theta)G_j(\theta)d\theta, \quad \forall\, i\in\{1,2,\ldots,K\}, \tag{14}$$

$$\mathbf{M} = \sum_{j=1}^{K}\int_\theta G_i(\theta)G_j(\theta)d\theta, \quad \forall\, i\in\{1,2,\ldots,K\}, \tag{15}$$

$$\mathbf{H}_\theta = \sum_{j=1}^{K} G_i(\theta)\Big\{\Big(\max(c_{\theta\, j+\frac{1}{2}},0)+\min(c_{\theta\, j-\frac{1}{2}},0)\Big)G_j(\theta)+\min(c_{\theta\, j+\frac{1}{2}},0)G_{j+1}(\theta)+ \max(c_{\theta\, j-\frac{1}{2}},0)G_{j-1}(\theta)\Big\} + \int_\theta\frac{dG_i(\theta)}{d\theta}c_\theta(\mathbf{r},t,\theta)G_j(\theta)d\theta, \quad \forall\, i\in\{1,2,\ldots,K\}. \tag{16}$$

Here $\mathbf{A}$ is a vector of matrices, with $\mathbf{A_x},\mathbf{A_y}$ being the $K\times K$ angular streaming matrices in the x- and y-direction respectively. $\mathbf{M}$ is the $K\times K$ angular mass matrix and $\mathbf{H}_\theta$ the $K\times K$ angular refraction matrix.

2.3. Temporal discretisation

To discretise time, a first-order implicit finite difference scheme is used. If the continuous time–space is divided into discrete timesteps $\{t, t+1\ldots\}$, then the action balance equation can be expressed as

$$\frac{\partial N(\mathbf{r},t,\theta)}{\partial t}+\mathcal{L}\Big(N(\mathbf{r},t,\theta)\Big)\approx\frac{N(\mathbf{r},\theta)^{t}-N(\mathbf{r},\theta)^{t-1}}{\Delta t}+\mathcal{L}\Big(N(\mathbf{r},\theta)^{t}\Big), \tag{17}$$

where, to avoid lengthy equations, $\mathcal{L}$ is an operator representing the last two terms of (6). Applying this to the vector form of the angularly discretised system (11) gives

$$\mathbf{M}\frac{1}{\Delta t}\mathbf{N}(\mathbf{r})^{t}+\Big(\mathbf{A}c_{g}(\mathbf{r})^{t}\Big)\cdot\nabla\mathbf{N}(\mathbf{r})^{t}+\nabla\cdot\Big(\mathbf{A}c_{g}(\mathbf{r})^{t}\Big)\mathbf{N}(\mathbf{r})^{t}+\mathbf{H}_{\theta}(\mathbf{r})^{t}\mathbf{N}(\mathbf{r})^{t}=\mathbf{M}\frac{1}{\Delta t}\mathbf{N}(\mathbf{r})^{t-1}. \tag{18}$$

2.4. Spatial discretisation

Owing to the hyperbolic nature of the energy balance equation, schemes that exhibit upwind bias are necessary such as discontinuous finite element, Petrov–Galerkin or Taylor–Galerkin methods. As an alternative, here the spatial dimensions are discretised with a sub-grid scale finite element method (SGS). The SGS method combines the benefits of continuous Galerkin formulations, i.e. low computational cost, with discontinuous Galerkin formulations, i.e. accuracy and stability. This is based on the work of Buchan et al. [45], who used this methodology for the spatial discretisation of the Boltzmann transport equation.

A full description of the SGS method is beyond the scope of this work, but a brief description is presented below. To formulate the model, the spatial domain $V\subset\mathbb{R}^{2}$ is partitioned into a set of disjoint sub-domains $V_{j},\ j\in\{1,2,\ldots,\eta\}$. The full solution $\mathbf{N}(\mathbf{r})$ is then decomposed into two components

$$\mathbf{N}(\mathbf{r})=\mathbf{\Phi}(\mathbf{r})+\mathbf{\Theta}(\mathbf{r}), \tag{19}$$

where $\mathbf{\Phi}$ and $\mathbf{\Theta}$ represent the coarse scale (continuous) and fine SGS scale (discontinuous) components of the solution respectively. The coarse component's approximation lies in a continuous finite element space, spanned by the continuous trial functions $P_{j},\ j\in\{1,2,\ldots,\eta_{P}\}$,

$$\mathbf{\Phi}(\mathbf{r})\approx\tilde{\mathbf{\Phi}}=\sum_{j=1}^{\eta_{P}}\mathbf{P}_{j}(\mathbf{r})\mathbf{\Phi}_{\mathbf{j}}, \tag{20}$$

while the fine scale approximation lies in a discontinuous finite element space, spanned by the discontinuous trial functions $Q_{j},\ j\in\{1,2,\ldots,\eta_{Q}\}$,

$$\mathbf{\Theta}(\mathbf{r})\approx\tilde{\mathbf{\Theta}}=\sum_{j=1}^{\eta_{Q}}\mathbf{Q}_{j}(\mathbf{r})\mathbf{\Theta}_{\mathbf{j}}. \tag{21}$$

Given that $\mathbf{\Phi}$ and $\mathbf{\Theta}$ are angular vectors of size K, the terms $\mathbf{P}_{j}$ and $\mathbf{Q}_{j}$ are $K\times K$ diagonal matrices, containing the spatial basis functions for each angular element. By weighting the equation using both sets of trial functions $\mathbf{P}_{i}$ and $\mathbf{Q}_{i}$ a system of $\eta_{P}+\eta_{Q}$ equations is formed:

$$\mathcal{A}\tilde{\mathbf{\Phi}}+\mathcal{B}\tilde{\mathbf{\Theta}}=\tilde{\mathbf{S}}_{\Phi}, \tag{22}$$

$$\mathcal{C}\tilde{\mathbf{\Phi}}+\mathcal{D}\tilde{\mathbf{\Theta}}=\tilde{\mathbf{S}}_{\Phi}, \tag{23}$$

where the sub-matrices are presented in Appendix A. If (23) is now multiplied by $\mathcal{D}^{-1}$, the subgrid scale solution becomes

$$\tilde{\mathbf{\Theta}}=-\mathcal{D}^{-1}\mathcal{C}\tilde{\mathbf{\Phi}}+\mathcal{D}^{-1}\tilde{\mathbf{S}}_{\Theta}. \tag{24}$$

Substituting this into (22) an expression for the resolved (coarse) solution is formed:

$$(\mathcal{A}-\mathcal{B}\mathcal{D}^{-1}\mathcal{C})\tilde{\mathbf{\Phi}}=-\mathcal{B}\mathcal{D}^{-1}\tilde{\mathbf{S}}_{\Theta}+\tilde{\mathbf{S}}_{\Phi}. \tag{25}$$

Thus the continuous coarse solution $\tilde{\mathbf{\Phi}}$ is solved using (25) and then (24) is utilised to calculate the discontinuous fine solution $\tilde{\mathbf{\Theta}}$. Finally the two components are added to get the full discontinuous solution $\mathbf{N}$ (19). In this work both the continuous and the discontinuous spaces are approximated with linear finite element basis functions ($P1$).

3. Wavelets

In section 2.2 an arbitrary angular discretisation is defined in (7), with the use of a set of angular basis functions G_{j}. As mentioned in section 1, in this work the angular dimension of the action balance equation is discretised with the use of wavelets. The section below outlines the construction of these angular basis functions G_{j}, for Haar wavelets. This allows for the calculation of the angular matrices of (13)–(16) and the construction of the linear system of (24)–(25).

3.1. Multiresolution analysis

In general, wavelets are constructed with the use of multiresolution analysis (MRA) [46]. First a MRA is built and then the wavelet family can be constructed with the desired criteria. Thus, a small introduction to MRA is necessary. A multiresolution analysis is a nested sequence V_j, $j \in \mathbb{Z}$, of subspaces of $L^2(\mathbb{R})$, the set of all Lebesgue integrable functions on the real line, i.e. the collection of functions $f : \mathbb{R} \to \mathbb{R}$ such that $\int_{\mathbb{R}} f^2 d\mathbb{R} < \infty$. The basic properties for a MRA are,

1. $V_j \subseteq V_{j+1}$, $j \in \mathbb{Z}$;
2. $\bigcup_{j\in\mathbb{Z}} V_j$ is dense in $L^2(\mathbb{R})$;
3. At each level j, there exists a set of scaling functions $\phi_{j,k}$, $k \in K'(j)$ for some index set K', for which the set $\{\phi_{j,k} \mid k \in K'(j)\}$ forms a Riesz basis of V_j.

For numerical applications, these nested spaces can be used to approximate any function $f \in L^2(\mathbb{R})$, by projecting f onto $f_j \in V_j$. In particular, using the scaling functions which span V_j the approximation becomes,

$$f \approx f_j = \sum_k \alpha_k \phi_{j,k}, \tag{26}$$

where j is the level of the space, k is the index number of the scaling functions for each level and α_k are the expansion coefficients which need to be determined. The accuracy of the expansion is then governed by the choice of j, as property 2 from above states that f can be fully recovered in the limit $j \to \infty$.

3.2. Wavelet construction

Using the MRA, wavelets can be generated as a basis for the spaces W_j that complement V_j in V_{j+1}, i.e. $V_{j+1} = V_j \oplus W_j$. These are denoted as $\{\psi_{j,m} \mid m \in M(j)\}$, for some index set $M(j)$. Given that W_j is contained in V_{j+1}, so are the wavelet functions, i.e. $\psi_{j,m} in W_j \subset V_{j+1}$. This means that the wavelet functions can be constructed as a combination of the scaling functions spanning V_{j+1},

$$\psi_{j,m} = \sum_{k\in K(j+1)} v_{j,m,k} \phi_{j+1,k}. \tag{27}$$

Recursively applying the relationship $V_j = V_{j-1} \oplus W_{j-1}$ gives,

$$V_j = V_{j-1} \oplus W_{j-1} = V_{j-2} \oplus W_{j-2} \oplus W_{j-1} = \ldots = V_l \oplus_{n=l}^{j-1} W_n. \tag{28}$$

Finally combining this with property 2 above yields,

$$L^2(\mathbb{R}) = V_l \oplus_{n=l}^{\infty} W_n. \tag{29}$$

Equation (29) defines a basis for $L^2(\mathbb{R})$ using the scaling functions in V_l, where l is the starting level for the scaling functions, and the wavelet functions spanning W_n, $n \in \{l, l+1, \ldots, \infty\}$. Thus any function $f \in L^2(\mathbb{R})$ can be also expressed as combination of scaling functions and wavelets as

$$f = \sum_{k\in K(l)} \alpha_k \phi_{l,k} + \sum_{n=l}^{\infty} \sum_{k\in M(n)} \beta_{n,k} \psi_{n,k}. \tag{30}$$

Finally, projecting f onto $f_j \in V_j \subset L^2(\mathbb{R})$ yields

$$f \approx f_j = \sum_{k\in K(l)} \alpha_k \phi_{l,k} + \sum_{n=l}^{j-1} \sum_{k\in M(n)} \beta_{n,k} \psi_{n,k}. \tag{31}$$

3.3. Haar wavelets

Before moving on to the presentation of Haar wavelets, the space V_j must be defined in terms of the governing equation. Wavelets are used for the angular discretisation of the action balance equation and thus, V_j represents the angular domain $\theta \in \{0, 2\pi\}$. In particular given a specific level l of the MRA, V_l is split into 2^l subdivisions (Fig. 2).

The Haar scaling functions, are piecewise constant functions within those intervals:

$$\phi_{l,k}(x) = \begin{cases} 1 & \text{if } x \in i_k, \\ 0 & \text{otherwise.} \end{cases} \tag{32}$$

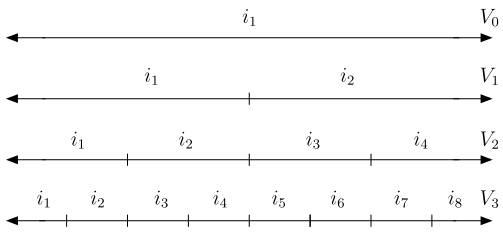

Fig. 2. Haar wavelet MRA of the 2π angular domain. Each space V_l has 2^l subdivisions.

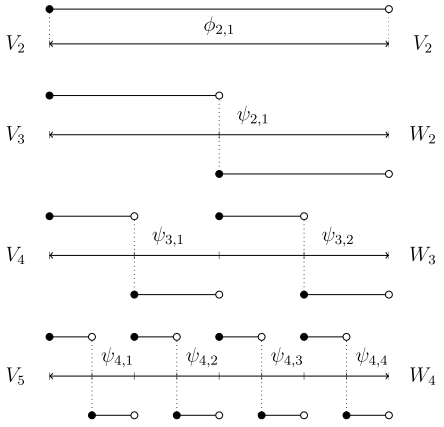

Fig. 3. Example of Haar wavelets on a quadrant of the 2π angular domain. Each V_j space (denoted on the left) is reproduced by $V_j = V_l \oplus_{n=2}^{j-1} W_n$ (denoted on the right). Space V_5 can be thus reproduced by $V_5 = V_2 \oplus W_2 \oplus W_3 \oplus W_4$.

The Haar wavelets are defined as

$$\psi_{n,k}(x) = \begin{cases} 1 & \text{if } x \in i_{2k-1}, \\ -1 & \text{if } x \in i_{2k}, \\ 0 & \text{otherwise}, \end{cases} \tag{33}$$

where $n \in \{l, l+1, \ldots, j-1\}$ for V_j. The hierarchy of scaling functions and wavelets is presented in Fig. 3. First, the scaling functions are expanded on V_l. On the first wavelet level, W_l, wavelets span the same space as the scaling functions in V_l. For every new level the number of wavelets doubles and thus each new wavelet supports half the space.

If (32) and (33) are substituted into (31), the Haar wavelets' approximation for any function in $L^2(\mathbb{R})$ becomes,

$$f(x) \approx \sum_{k=1}^{2^l} \alpha_k \phi_{l,k}(x) + \sum_{n=l}^{j-1} \sum_{k=1}^{2^n} \beta_{n,k} \psi_{n,k}(x). \tag{34}$$

Equation (34) shows that any function in $L^2(\mathbb{R})$ can be approximated, with a linear combination of the scaling functions on level l and the wavelets on levels $n \in \{l, l+1, \ldots, j-1\}$. Henceforth, the Haar wavelet discretisation is referred to as $HW_{l,j}$. Following (28),

$$HW_{l,j} = V_l \oplus W_l \oplus W_{l+1} \oplus .... \oplus W_{j-1} = V_j. \tag{35}$$

$HW_{2,5}$ for instance has 2^2 scaling functions in V_2, 2^2 wavelets in W_2, 2^3 wavelets in W_3 and 2^4 wavelets in W_4. The resulting space is V_5 with a cumulative number of functions equal to $2^5 = 32$ (Fig. 3). To visualise the angular mesh, polar plots are used that show the position of the functions (middle point) for all the levels (Fig. 4).

3.4. Calculating the angular matrices

Equation (34) provides an expression for representing a function with Haar wavelets. Assuming the levels of the scaling functions and wavelets are known, the number of functions used for the projection is also known. Then (34) can be condensed to the single summation given in (7):

$$N(\mathbf{r}, t, \theta) \approx \sum_{j=1}^{K} N_j(\mathbf{r}, t) G_j(\theta), \tag{36}$$

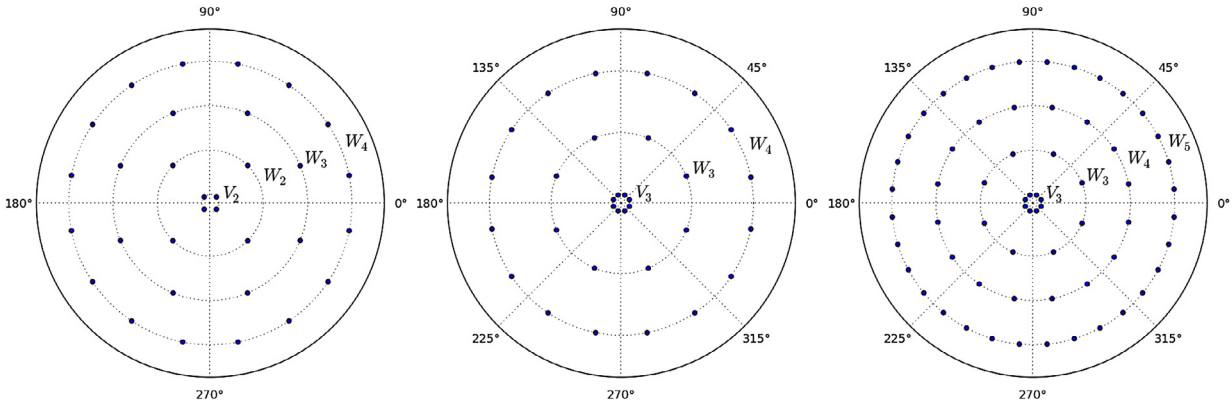

(a) $HW_{2,5} \to 32$ functions (b) $HW_{3,5} \to 32$ functions (c) $HW_{3,6} \to 64$ functions

Fig. 4. Polar plots for various Haar wavelet expansions. Each concentric circle represents the spaces: $\{V_l, W_l, W_{l+1}, \ldots, W_{j-1}\}$, for a $HW_{l,j}$ discretisation.

where N_j corresponds to the coefficients α, β and G_j to the functions ϕ and ψ of (7). Thus, scaling functions and Haar wavelets are now simply referred to as angular basis functions. Having the approximation for the angular dependence of the action density, all that is needed for the implementation of Haar wavelets is to calculate the angular matrices $\mathbf{A_x}$, $\mathbf{A_y}$, $\mathbf{M}$, $\mathbf{H}_\theta$ of (13)–(16), presented in section 2.2.

The vast majority of the available spectral wave models, use a finite difference approximation for the angular dimension. This is the equivalent of a cell centred finite element $P0$ discretisation. In the Boltzmann transport community this is known as discrete ordinates or SN [36]. If the angular matrices are calculated for this expansion then there exists a mapping operator $\mathcal{W}$, which maps the $P0$ space to the Haar space (both are piecewise constant, so the mapping is exact). The relationship is

$$\mathcal{W} N_W = N_{P0}, \tag{37}$$

where N_W and N_{P0} correspond to the action density approximated in the wavelet space and the $P0$ finite element space respectively. This mapping is applied to the angular matrices by pre-multiplying and post-multiplying by $\mathcal{W}^{\mathcal{T}}$ and $\mathcal{W}$ respectively as,

$$\mathbf{A_x^W} = \mathcal{W}^{\mathcal{T}} \mathbf{A_x^{P0}} \mathcal{W}. \tag{38}$$

The mapping matrix $\mathcal{W}$ is a square matrix of 1's, -1's and 0's. The use of the mapping operator simplifies the implementation of Haar wavelets, allowing them to be built on existing conventional frameworks. This is particularly useful for the calculation of the source terms (which are not included in this study).

4. Angular adaptivity

The application of anisotropic angular adaptivity, i.e. allowing the model to use a different angular discretisation for each spatial node, would normally require the reconstruction of the angular matrices (13)–(16) for each spatial node at each adaptive time-step. This can be a cumbersome task with a significant computational cost. Fortunately, the whole process can be easily simplified with the use of hierarchical expansions, such as the Haar wavelets used here. To make this clear, assume that a uniform expansion is applied globally. The coefficients of this expansion will be high at spatial nodes where the action density is high, and low in areas of low action density. As these coefficients get smaller a filter can be applied to zero them out and eventually remove them from the expansion. This is known as thresholding and used for data compression [41].

Applying this on an adaptive framework, the angular matrices are calculated for a uniform expansion, and for each spatial node only the coefficients that are above the threshold are added to the final system. This is where the real benefits from the use of Haar wavelets can be seen, due to their compact support; every time a new level gets added the support of the wavelets becomes smaller, focusing on more detail in the angular domain. Thus, an adaptive scheme with wavelets, allows for the concentration of angles on specific patches of the angular domain for each spatial node. This can significantly reduce the total number of basis functions. An added benefit of their hierarchical nature is that there is no need to interpolate between consecutive angular meshes. Projecting one adapted angular mesh onto the next simply consists of copying the existing angular coefficients over to the new angular mesh.

Thus, adapting in this framework simply consists of thresholding the angular coefficients every time the system gets assembled; the cost of adaptivity is negligible. The added cost comes from the use of wavelets. Compared to a $P0$ angular expansion, wavelets lead to denser angular matrices which means that for a uniform (non-adapted) expansion wavelets will be slower. However, Haar wavelets are still sparse, i.e. the extra cost is small, and the ability to have a variable angular mesh compensates for the added computational effort.

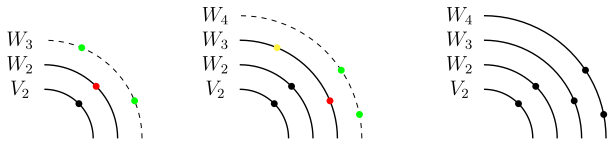

Fig. 5. Simplified example of the angular adaptive scheme. Starting from the left sketch the red basis function suggests that the respective next level (dashed line) basis functions (green) should be added, i.e. the wavelet coefficient is bigger than the tolerance $N_i > \tau$. The central sketch shows that one of the two newly added basis functions can be removed (yellow), while the other requires yet another level. The sketch on the right shows the final adapted system. (For interpretation of the references to color in this figure legend, the reader is referred to the web version of this article.)

4.1. Error measure

Haar wavelets provide a natural framework for identifying the regions where the action density is under- or over-resolved and hence the computational resolution should be altered. Each wavelet coefficient gets smaller as its importance becomes smaller. Thus, a magnitude-based error metric can be defined to indicate whether a wavelet coefficient is sufficiently small to be removed, or sufficiently large for its higher level hierarchical wavelets to be added. A simplified example is presented in Fig. 5.

Buchan et al. in [39] suggest that an appropriate error metric to be used is $N_j G_j A_j$ where N_j is the angular coefficient, G_j the basis function and A_j the support area of the basis function. However, for the Haar wavelets the basis functions switch between 1 and -1 and, after some initial results, the introduction of the area did not appear to have a significant impact. Thus, the error metric is implemented as

$$N_i > \tau. \tag{39}$$

If the angular coefficient is greater than a user-defined tolerance value τ then the error is considered significant, suggesting that more resolution should be added to this region, i.e. wavelets from the next level should be included. This could be repeated until enough levels have been added, such that none of the values for N_i are bigger than τ. However, in practice it is better to restrict the maximum number of levels. This means that both a $HW_{l,j_{\text{init}}}$ and a $HW_{l,j_{\max}}$ are defined, for the initial and finest possible discretisation respectively.

Finally a way to remove basis functions is also needed to ensure that there are no over-resolved regions. This threshold is set to $N_j < 0.01\tau$; every time an angular coefficient is smaller than 0.01τ it is removed. This does not apply to scaling functions.

4.2. Adaptive procedure

The overall adaptive procedure can be described as,

1. Start with a $HW_{l,j_{\text{init}}}$ discretisation, choose the maximum value $j_{\max}$ and a tolerance value for the error metric τ (39).
2. Run the non-adapted $HW_{l,j_{\text{init}}}$ system.
3. Loop every angular coefficient N_i for every spatial node and evaluate if they are within the error bounds,

$$\begin{aligned}
&\text{if} \quad N_i/\tau > 1 && \rightarrow \quad \text{If not at max level, add the next level functions for } N_i,\\
&\text{if} \quad N_i/\tau < 0.01 && \rightarrow \quad \text{If not a scaling function, remove } N_i,\\
&\text{if} \quad 0.01 \leq N_i/\tau \leq 1 && \rightarrow \quad \text{Keep } N_i.
\end{aligned}$$

4. Reassemble the system matrices (section 2.4), but only add the components of the angular matrices, corresponding to the adapted angular coefficients.
5. For stationary simulations, repeat the above process until convergence (i.e. the algorithm has stopped changing the angular mesh), or a maximum number of adapts has been reached.
6. For non-stationary applications, choose an adapt period to specify at which time-steps the adaptivity algorithm will be evoked.

Owing to the SGS method (section 2.4), the action density is discontinuous. The system that gets assembled, however, is continuous. A continuous error metric is, thus, necessary to apply to the adaptive algorithm. One way to derive this is by looping over the elements containing the same nodes and keeping the maximum values. Even though the frequency discretisation is omitted in this study, it is worth mentioning that in the case of multiple frequency groups a similar approach can be used to get a single error value for all groups. The frequency groups are looped over and the maximum value for the action density is kept for the error metric.

Finally a note on the use of the scaling functions. Given that $HW_{2,5}$ and $HW_{3,5}$ both result in the same number of basis functions (see Fig. 4), one could enforce the scaling functions to always start from the same level, i.e. level $l = 0$, and simplify the representation of wavelets to HW_j. However, the scaling functions are the only angular basis functions that

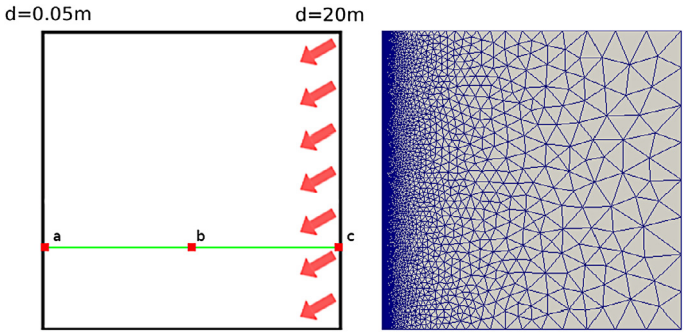

(a) Set-up. (b) Spatial mesh.

Fig. 6. Depth induced shoaling and refraction. Set-up explanation and spatial mesh. (For interpretation of the references to color in this figure, the reader is referred to the web version of this article.)

the adaptive algorithm cannot remove; thus by changing l, the minimum number of basis functions can be easily controlled giving an extra degree of freedom in the adaptive procedure. This could prove important in transient simulations when the wave field changes abruptly. The adaptive algorithm might not have enough time to resolve these areas and a minimum number of functions could be necessary to provide an accurate representation.

5. Numerical results

To present the adaptive framework and attempt to quantify its benefits two test cases are selected. The first one is a stationary depth-induced shoaling and refraction test case, routinely used to benchmark spectral wave models. This is a highly directional problem, where the angular resolution dominates the errors. The second is an idealised deep water propagation scenario which is a standard test case for studying the "Garden Sprinkler Effect" (GSE). The GSE is a direct result of the angular discretisation and thus highly sensitive to the angular resolution. Since no effort has been spent to optimise the code, the results are not compared against other spectral wave models. Instead Haar adaptivity is compared against uniform resolutions within the same code to demonstrate the advantages of the proposed numerical framework.

5.1. Depth-induced shoaling-refraction

A plane beach front is considered, represented by a 4000 m $\times$ 4000 m domain, with a bathymetric slope of 1 : 200. A long wave enters from the deep eastern boundary with $d = 20$ m, at an angle of 210° (measured counter-clockwise for the positive x-axis), propagating towards the shallow western boundary with $d = 0.05$ m (Fig. 6(a)). As the wave encounters shallower waters, it slows down, causing its wave length to decrease and, thus, its wave height to increase (shoaling). To account for this, the spatial mesh has a variable element size, starting from an edge length of 600 m and going down to 20 m (Fig. 6(b)). As different parts of the wave-train travel with different speeds, the wave also turns (refraction).

To test shoaling and refraction, a monochromatic wave is set-up with a significant wave height of 1 m, a frequency of 0.1 Hz and a $\cos^{500}(\theta)$ directional distribution (this results in a directional width of $\sigma_\theta = 2.5°$, where σ_θ is the standard deviation of the directional distribution [47]). The significant wave height and the angle of direction can be compared to,

$$\frac{H^2}{H_i^2} = \frac{c_{gi}\cos(\theta_i)}{c_g\cos(\theta)}, \tag{40}$$

$$\frac{\sin(\theta)}{\sin(\theta_i)} = \frac{c}{c_i}, \tag{41}$$

where H is the significant wave height, θ is the direction, c_g and c the group and phase velocity respectively, while i denotes the incident value.

First the $P0$ angular discretisation is tested with 400 angular degrees of freedom ($\Delta\theta = 0.9°$). The results of the simulation plotted along the $y = 1000$ m line (green line of Fig. 6(a)) are presented in Fig. 7, showing good agreement for both shoaling and refraction.

A refraction convergence test for the uniform P0 angular mesh is presented in Fig. 8. For each simulation the number of angles is doubled and the discrete root-mean-square (RMS) error plotted, compared to (41), along the $y = 1000$ m line. This is presented by the blue line in Fig. 8, where first order convergence $(p + 1)$ is achieved. In these simulations, the angles are uniformly applied to all the spatial nodes of the domain. However the directional width is narrow which means that as the angular mesh is refined, a very small number of the angles have a non-zero action density.

Adaptive Haar wavelets are now used and compared to the uniform $P0$ results. For the application of angular adaptivity in stationary simulations it is advised to start with a coarse angular mesh, i.e. at the scaling function level. Each adaptive iteration then gradually introduces new angular basis functions, until the system converges, i.e. the algorithm stops changing

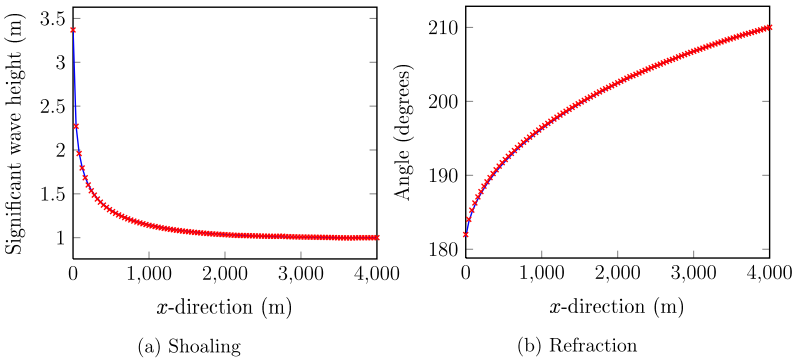

Fig. 7. Validation for depth induced shoaling and refraction. A $P0$ angular discretisation with 400 angles compared against the analytical solutions of (40) and (41).

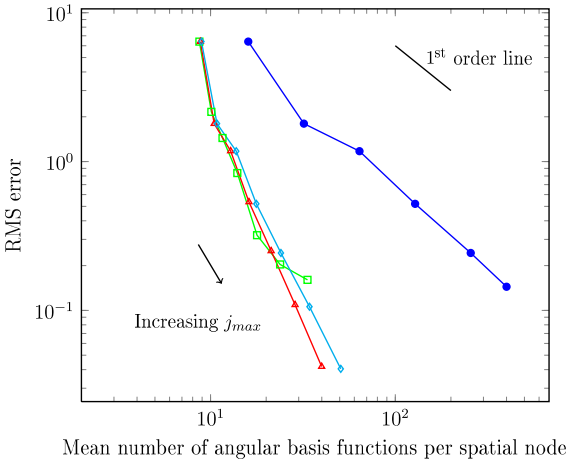

Fig. 8. Depth induced refraction. Convergence tests for uniform $P0$ and $HW_{3,j}$, $j_{\max} \in \{4, 5, 6, 7, 8, 9, 10\}$, adaptive discretisations for various tolerances: $\tau = 1$, $\tau = 10^{-1}$, $\tau = 10^{-2}$. The $HW_{3,j}$ points correspond to the results after the adaptive algorithm converges. (For interpretation of the references to color in this figure, the reader is referred to the web version of this article.)

the angular mesh and there is no change in the action density. This way the computational costs are small and only grow according to the errors of the simulation. In practice the convergence criteria should be relaxed to a percentage of the change of the action density (or the significant wave height), as after a point the change in the action density will be too small to justify the extra cost of re-running the system.

For each $HW_{l,j}$ simulation the scaling function and initial levels are $j_{\text{init}} = l = 3$. The maximum level $j_{\max}$ is increased and the RMS error is plotted, compared to (41), along the $y = 1000$ m line. The results for a $HW_{3,j}$, $j_{\max} \in \{4, 5, 6, 7, 8, 9, 10\}$, discretisation with tolerances $\tau \in \{1, 10^{-1}, 10^{-2}\}$ are presented in Fig. 8.

For a tolerance $\tau = 1$, as $j_{\max}$ increases the errors appear to level out. As new levels are introduced, the values of the action density coefficients N_i become smaller, until they are ignored by the adaptive algorithm. Thus, even though $j_{\max}$ increases there is not enough resolution to represent the directional distribution of the action density and the errors stop decreasing. This is a clear indication that the selected tolerance value is too large. Decreasing the tolerance to $\tau = 10^{-1}$ amends this and produces errors comparable to the uniform resolution discretisation. A further reduction of the tolerance to $\tau = 10^{-2}$ produces similar errors to $\tau = 10^{-1}$, with a higher number of angular basis functions. This means that as the tolerance is further decreased, new basis functions are introduced that do not have a significant impact on the errors of the simulation. Indeed, for an infinitesimal value of τ adaptivity should uniformly add all the angular basis functions producing the same results as the uniform $P0$ discretisation. It is the balance between accuracy and computational costs that ultimately defines the tolerance value.

In terms of the computational degrees of freedom, the adaptive $HW_{3,j}$ discretisations consistently use fewer degrees of freedom compared to the uniform $P0$ discretisations. The error level for a $P0$ angular discretisation with 128 angles is achieved with almost an order of magnitude less degrees of freedom by the adaptive $HW_{3,7}$ discretisation. Moving towards finer angular meshes, this difference becomes even bigger, showing the advantages of angular adaptivity for high fidelity results.

To see how this translates in computational times, the results with a tolerance $\tau = 10^{-1}$ are isolated and the errors against the run-times are plotted in Fig. 9. These are the results after each simulation has converged. For the same error

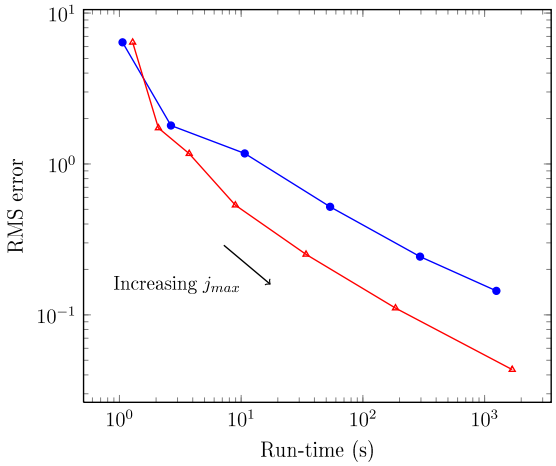

Fig. 9. Depth induced refraction. Convergence tests for uniform $P0$ with $\{16, 32, 64, 128, 256, 400\}$ angles —●— and $HW_{3,j}$, $j_{\max} \in \{4, 5, 6, 7, 8, 9, 10\}$, adaptive discretisations for a tolerance $\tau = 10^{-1}$ —△—. The $HW_{3,j}$ points correspond to the results after the adaptive algorithm converges.

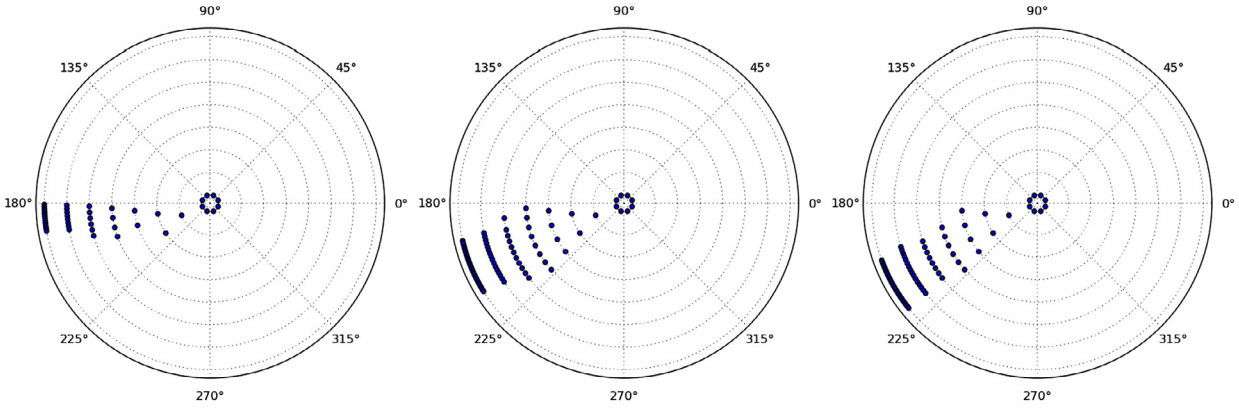

(a) Point a (b) Point b (c) Point c

Fig. 10. Polar plots for a $HW_{3,10}$ discretisation for points: $a = (0\text{ m}, 1000\text{ m})$, $b = (2000\text{ m}, 1000\text{ m})$, $c = (4000\text{ m}, 1000\text{ m})$ in Fig. 6(a).

levels adaptive $HW_{3,j}$ discretisations run consistently faster, with differences approaching an order of magnitude for fine resolutions. For the uniform $P0$ angular discretisation with 128 angles, the same error is achieved by the $HW_{3,7}$, six times faster. It is worth noting that the $HW_{3,7}$ converges after ten adapts, i.e. solving ten times the adapted system is six times faster than solving the uniform system once.

Finally in Fig. 10 the polar wavelet plots for a $HW_{3,10}$ discretisation with a tolerance of $\tau = 10^{-1}$ are presented for three different locations with coordinates: (0 m, 1000 m), (2000 m, 1000 m), (4000 m, 1000 m), or point a, b and c in Fig. 6(a). As the wave propagates from point c to point a, its mean direction shifts from 210° to 180°. The angular basis functions follow the change of the mean direction refining only the patches of the angular domain that are active for each spatial node.

5.2. Deep water propagation

An inherent problem of the phase-space discretisation is the spurious separation of energy into the discretised bins. This is called the "Garden Sprinkler Effect" and has been extensively studied in [48,49,20]. (In the Boltzmann transport community this is known as the ray effect.) To showcase this effect in the angular dimension, a large spatial domain (4000 km × 4000 km) is simulated, with a monochromatic wave propagating over a long distance in deep water ($d = 10\,000$ m). For the spatial discretisation a structured triangle mesh is used, with an element edge length of 67 km (Fig. 11(a)). The initial wave field, located 500 km from the lower and left side has a Gaussian distribution in space, with a significant wave height of $H_s = 2.5$ m and a standard deviation of 150 km (Fig. 11(b)). Its mean direction is 30° with an angular distribution of $\cos^2(\theta)$ and a frequency of 0.1 Hz. The simulation is time-dependent and runs for 5 days with a time-step of 600 s.

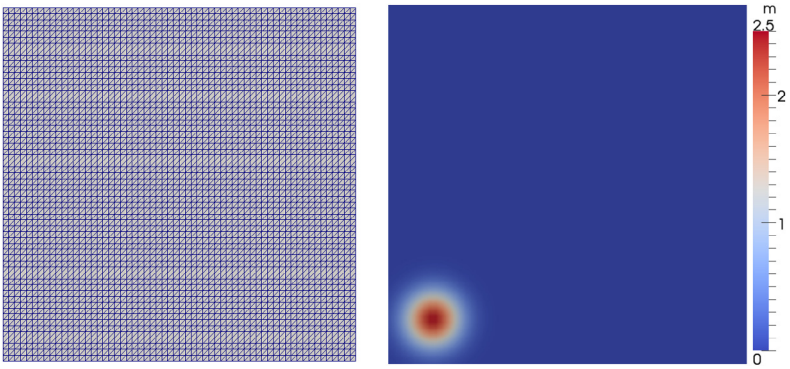

(a) Spatial mesh (b) Initial field

Fig. 11. Spatial mesh and initial conditions for the deep water propagation test case.

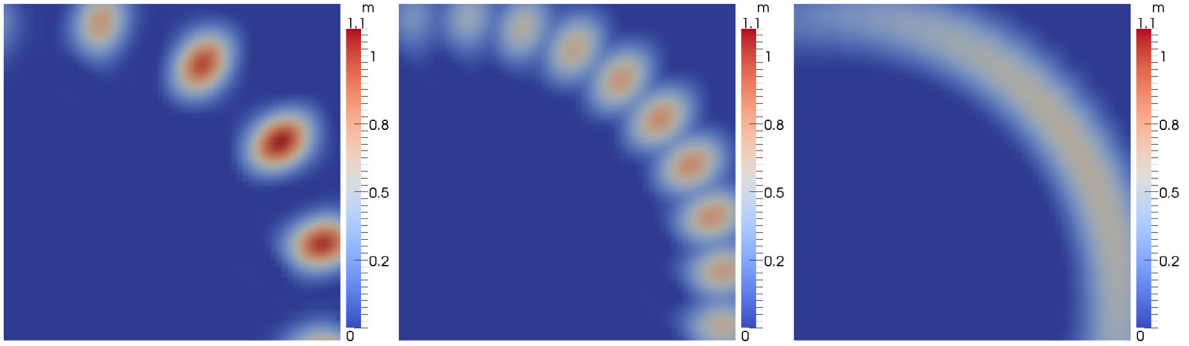

(a) $P0$ - 16 angles (b) $P0$ - 32 angles (c) $P0$ - 64 angles

Fig. 12. Significant wave height after 5 days of deep water propagation, for a $P0$ angular discretisation with various angular resolutions.

In Fig. 12, the results at the final timestep for a $P0$ angular discretisation with 16, 32 and 64 basis functions are presented. As the wave propagates, it breaks up into the paths of the prescribed directions; the coarser the angular discretisation, the more intense the GSE will be. This is also connected to the numerical diffusion of the spatial discretisation. Higher order schemes have a lower numerical diffusion, which intensifies the GSE. This essentially means that increasing the resolution in geographic space makes the GSE worse.

The obvious solution is to increase the number of angles. However, in the multidimensional framework of the action balance equation increasing the number of angles globally significantly affects the computational costs. With a finite element expansion, as the one presented here, doubling the angular basis functions quadruples the size of the angular matrices. This increased computational cost for finer angular resolutions, led to the use of a diffusion correction term by [48], which smears out the action density depending on the wave age. By knowing how much the wave field has propagated, it can be spread accordingly to alleviate the GSE. Calculating the wave age, however, is costly, leaving the age as a tunable coefficient, which introduces inaccuracies.

Here, as an alternative, angular adaptivity is used, to increase the accuracy of the solution while keeping the computational cost at a minimum. A $HW_{2,6}$ discretisation is applied, with a tolerance value of $\tau = 10^{-6}$. This introduces a maximum of $2^6 = 64$ basis functions, making the results comparable to the uniform $P0$ with 64 angles. By starting the simulations at the scaling function level, as in the stationary example, the initial $\cos^2(\theta)$ distribution is only represented by 4 angles. This of course introduces errors which then propagate throughout the simulation. Thus, the simulation starts at the maximum angular discretisation $j_{\text{init}} = j_{\text{max}}$. (An alternative would have been to be able to adapt a few times at the first timestep before propagating in time.) Given that the cost of adapting is negligible, adaptivity is activated at each time-step.

In Fig. 13 the adaptive run is presented at various time levels, while Fig. 14 shows the difference between the significant wave height for the $HW_{2,6}$ and $P0-64$ angles runs. The results are readily comparable, with differences in the order of mm.

However, capturing the solution is only part of the goal, as the objective is the reduction of the computational cost. To showcase this, the angular mesh, or the distribution of the number of angular basis functions in space, is presented in Fig. 15. The angular mesh can be seen to be following the propagation of the wave field, surrounding the area around it. It is worth observing that the maximum errors in Fig. 14 occur at the edges of this area. The smaller the prescribed tolerance, the bigger the region of increased adapted angles will be and thus the smaller the error.

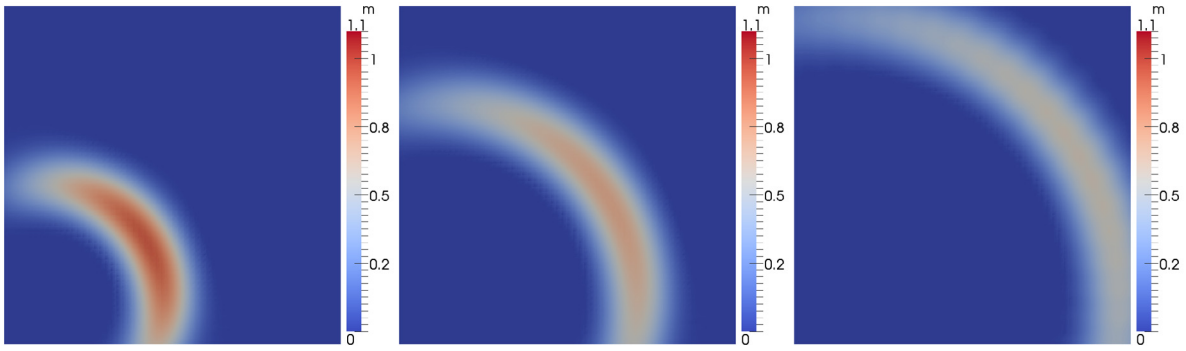

(a) $t = 2$ days. (b) $t = 3.5$ days. (c) $t = 5$ days.

Fig. 13. Significant wave height for an adaptive $HW_{2,6}$ discretisation with tolerance $\tau = 10^{-6}$ at several time levels.

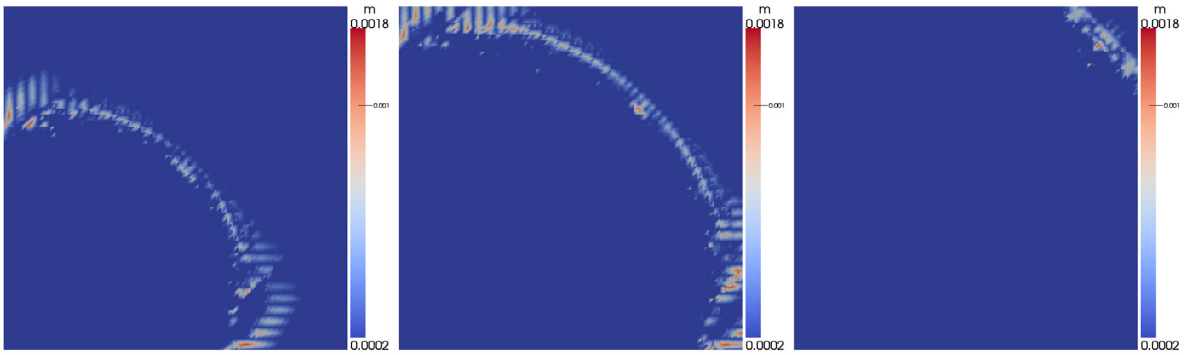

(a) $t = 2$ days. (b) $t = 3.5$ days. (c) $t = 5$ days.

Fig. 14. Absolute difference in significant wave height between a $P0 - 64$ angle and an adaptive $HW_{2,6}$ discretisation with tolerance $\tau = 10^{-6}$ for various time levels. Colorbar in logarithmic scale.

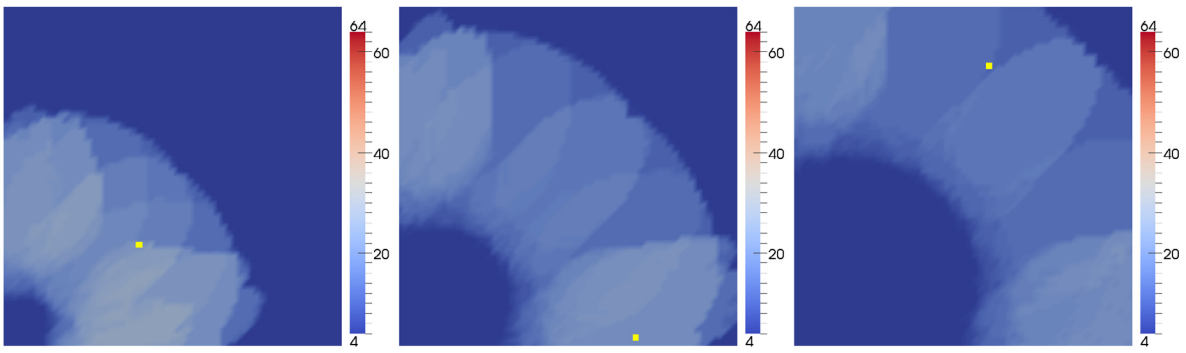

(a) $t = 2$ days. (b) $t = 3.5$ days. (c) $t = 5$ days.

Fig. 15. Angular mesh, i.e. number of angular basis functions, for a $HW_{2,6}$ discretisation with tolerance $\tau = 10^{-6}$ at various time levels. The polar plots for the points denoted by the yellow dots are presented in Fig. 16. (For interpretation of the references to color in this figure legend, the reader is referred to the web version of this article.)

Finally in Fig. 16 the polar plots for the three geographical points denoted by the yellow dots in Figs. 15(a)–(c), are presented at their respective time levels. For each point, the wave field has a different mean direction and directional distribution. Adaptivity adjusts the number and position of angular basis functions accordingly.

To better quantify the savings in the computational costs from using angular adaptivity a convergence test is now presented. First the $P0$ angular discretisation is tested. With 300 angles used to construct the reference solution, the number of angles is gradually increased and the $l2$ norm of the significant wave height for the final timestep is plotted against the run-time. This is presented in the blue line of Fig. 17.

For the adapted runs, a $HW_{2,j}$, $j_{\max} \in \{3, 4, 5, 6, 7, 8\}$, discretisation is used with tolerances $\tau \in \{10^{-6}, 10^{-7}, 10^{-8}\}$. The results are presented in Fig. 17. As $j_{\max}$ is increased the maximum number of basis functions is doubled and the $HW_{2,j}$

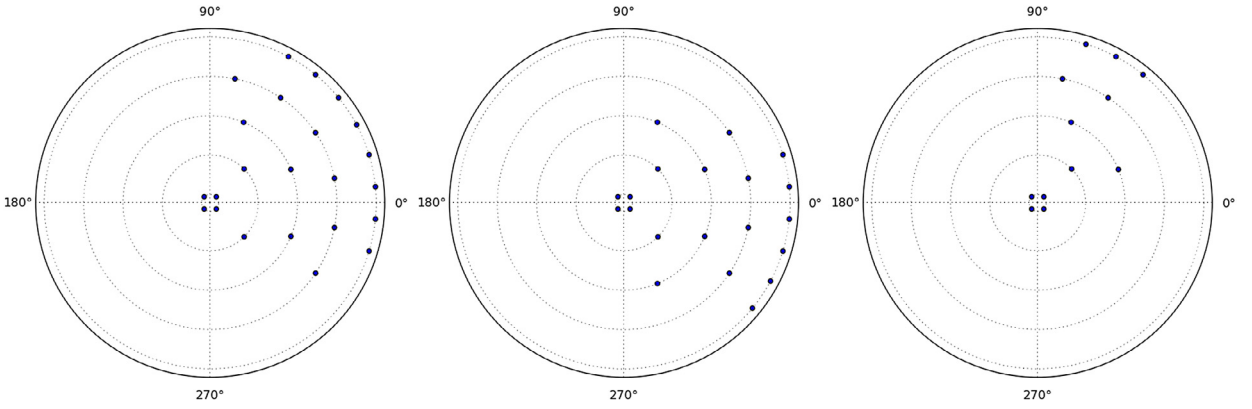

(a) $t = 2$ days. (b) $t = 3.5$ days. (c) $t = 5$ days.

Fig. 16. Polar plots of a $HW_{2,6}$ discretisation for the points in Fig. 15, at their respective time levels.

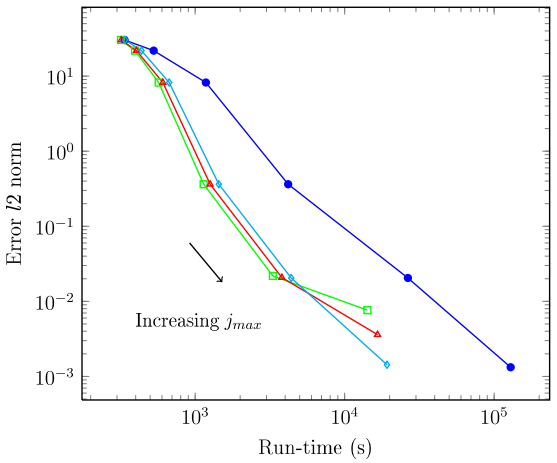

Fig. 17. Error against run-time for the deep water propagation test case. Results for $P0$ with $\{8, 16, 32, 64, 128, 256\}$ angles —●— and $HW_{2,j}$, $j_{\max} \in \{3, 4, 5, 6, 7, 8\}$, for tolerances: $\tau = 10^{-6}$ —□—, $\tau = 10^{-7}$ —△—, $\tau = 10^{-8}$ —◇—. Each point corresponds to the error compared to a uniform $P0$ discretisation with 300 angles, at the final time level. (For interpretation of the references to color in this figure, the reader is referred to the web version of this article.)

lines move towards higher run-times and smaller errors. Using a smaller tolerance value, adaptivity inserts more angles and thus the run-times are higher. However, up to $j_{\max} = 7$ the errors are the same for all tolerances, i.e. the extra angular basis functions that are inserted do not significantly impact the error. A significant difference can only be seen for the last value of $j_{\max} = 8$. This is the point where the accuracy of the solution is comparable to the tolerance limit and thus decreasing the tolerance produces better results. For the case of $\tau = 10^{-8}$ the highest value of $j_{\max} = 8$ gives the same error values as the respective uniform $P0$ runs. This is a useful guide to how the tolerance should be tuned depending on the desired accuracy.

The adaptive simulations are consistently faster compared to the uniform resolution ones. The same error produced by a uniform $P0$ angular discretisation with 128 angles is achieved almost an order of magnitude faster by the $HW_{2,7}$ adaptive discretisation. As the angular resolutions increase this difference becomes bigger. This is due to the reduced number of degrees of freedom, as is evident in Fig. 18, where the mean number of angular basis functions for a tolerance of $\tau = 10^{-6}$ is plotted at each time level. At the first time level, the simulation starts with the maximum number of angles so as to accurately represent the initial angular distribution. After the first adapt, the mean number of basis functions immediately drops and the simulations run consistently with up to an order of magnitude fewer degrees of freedom. As the wave field propagates it spreads covering a larger computational area. Thus, the degrees of freedom increase towards higher time levels, only to decrease again when parts of the wave field exit the domain. This constant adjustment of the degrees of freedom ensures that the computational costs are always optimised depending on the desired accuracy.

6. Conclusions

Due to the multidimensional nature of the action balance equation, the computational costs associated with its solution renders the use of high fidelity discretisations expensive and inefficient. This means that in realistic domains, the number

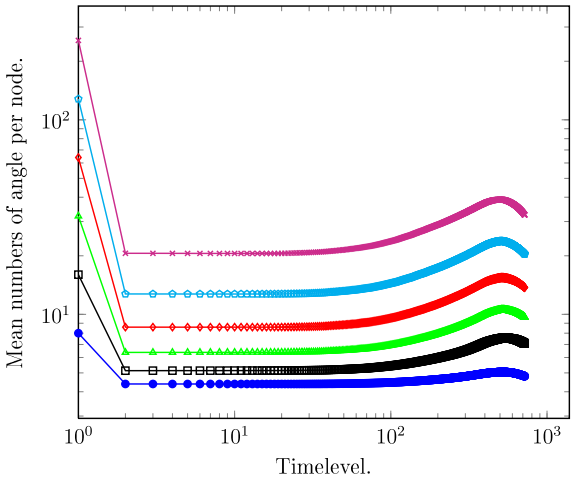

Fig. 18. Mean number of angular basis functions against timelevel for the deep water propagation test case. $HW_{2,3}$ —●—, $HW_{2,4}$ —□—, $HW_{2,5}$ —△—, $HW_{2,6}$ —◇—, $HW_{2,7}$ —○—, $HW_{2,8}$ —×—, for a tolerance of $\tau = 10^{-6}$.

of angles used needs to be kept small. In general, however, sea surface wind-wave fields are directional and thus in most cases the majority of angular degrees of freedom do not significantly impact on the accuracy of the solution. What is more, the mean direction of the wave field is constantly changing and the rate of this change is subject to external forces, such as the wind, currents and the bathymetric slope. Hence, a-priori estimation of the required angular mesh resolution is challenging.

To resolve this problem, this paper introduces a new framework for applying angular adaptivity in spectral wave models. The method employs hierarchical angular expansions, using Haar wavelets to represent the angular dependence of the action density. The adaptive procedure uses the hierarchy and compact support of wavelets to locate the areas on the angular mesh that are under-resolved and increase the number of angular functions to locally refine the resolution. At the same time, areas that are over-resolved are identified and functions removed to decrease the global degrees of freedom without negatively impacting on the accuracy. By controlling the minimum and maximum number of basis functions, as well as the tolerance for the error metric the balance between errors and computational costs is easily managed.

The method is applied to a steady state depth induced shoaling-refraction test case, as well as a transient large scale propagation test case. The adaptive results are verified against a uniform resolution discretisation and the gains in terms of computational degrees of freedom and run-times are quantified.

Wavelets are constantly rearranged for each geographic point following the mean direction and capturing the directional distribution of the wave field. Thus, the same error levels, compared to a uniform expansion, are achieved in both cases with lower computational costs and faster run times. In particular, for an angular resolution of 128 angles, adaptivity runs with an order of magnitude less degrees of freedom compared to the uniform resolution. This translates in six times faster run-times for the shoaling-refraction test case and almost an order of magnitude faster run times for the large scale propagation test case. This refers to the total run-times including both the linear solves and the adapt process. The difference widens as the angular mesh is further refined, showing the advantage of adaptivity for high fidelity results.

In all the results presented the objective is to show that adaptive wavelets can reproduce the same errors as the equivalent uniform resolution angular meshes. Thus, the convergence criteria are strict and the tolerance limits low. In practical simulations the convergence criteria and tolerance limits need to be linked to the change of the significant wave height, which will result in fewer angular basis functions and, thus, faster run-times. Speed-ups can also be achieved by optimising the scheme, such as exploiting the sparsity of the angular matrices for the mapping.

Haar wavelets provide an effective framework for applying anisotropic angular adaptivity, refining the angular resolution according to the desired accuracy while at the same time reducing the computational costs. This can push spectral wave models towards higher resolutions and help bridge the gap between coarse large scale and fine coastal zone simulations.

Acknowledgement

This work would not have been possible without the help of AMCG's Radiation group at Imperial College, including but not limited to Steven Dargaville, Richard P. Smedley-Stevenson and Paul Smith. A. Adam would like to acknowledge PhD funding from Imperial College London. The authors would also like to acknowledge the support of UK's Engineering and Physical Sciences Research Council under projects EP/J010065/1, EP/J002011/1 and EP/M022684/1. The research leading to these results has also received funding from the European Union Seventh Framework Programme (FP7/2007–2013) under Grant agreement n° 603663 for the research project PEARL (Preparing for Extreme And Rare events in coastaL regions).

Appendix A. Sub-grid scale matrices

The sub-grid scale matrices $\mathcal{A}, \mathcal{B}, \mathcal{C}, \mathcal{D}$, are,

$$\mathcal{A}_{i,j} = \int_V \mathbf{P}_i \mathbf{M} \frac{1}{\Delta t} \mathbf{P}_j dV + \int_V \mathbf{P}_i \mathbf{H}_\theta(\mathbf{r})^{t,\sigma} \mathbf{P}_j dV + \int_V \mathbf{P}_i \mathbf{H}_f(\mathbf{r})^{t,\sigma} \frac{1}{\Delta f} \mathbf{P}_j dV + \int_\Gamma \mathbf{P}_i \left[\left(\mathbf{A} c_g(\mathbf{r})^{t,\sigma} + \mathbf{M}\mathbf{u}(\mathbf{r})^{t,\sigma} \right) \cdot \mathbf{n} \right] \mathbf{P}_j d\Gamma - \int_V \nabla \mathbf{P}_i \cdot \left(\mathbf{A} c_g(\mathbf{r})^{t,\sigma} + \mathbf{M}\mathbf{u}(\mathbf{r})^{t,\sigma} \right) \mathbf{P}_j dV \tag{A.1}$$

$$\mathcal{B}_{i,j} = \int_V \mathbf{P}_i \mathbf{M} \frac{1}{\Delta t} \mathbf{Q}_j dV + \int_V \mathbf{P}_i \mathbf{H}_\theta(\mathbf{r})^{t,\sigma} \mathbf{Q}_j dV + \int_V \mathbf{P}_i \mathbf{H}_f(\mathbf{r})^{t,\sigma} \frac{1}{\Delta f} \mathbf{Q}_j dV - \int_V \nabla \mathbf{P}_i \cdot \left(\mathbf{A} c_g(\mathbf{r})^{t,\sigma} + \mathbf{M}\mathbf{u}(\mathbf{r})^{t,\sigma} \right) \mathbf{Q}_j dV \tag{A.2}$$

$$\mathcal{C}_{i,j} = \int_{V_e} \mathbf{Q}_i \mathbf{M} \frac{1}{\Delta t} \mathbf{P}_j dV + \int_{V_e} \mathbf{Q}_i \mathbf{H}_\theta(\mathbf{r})^{t,\sigma} \mathbf{P}_j dV + \int_{V_e} \mathbf{Q}_i \mathbf{H}_f(\mathbf{r})^{t,\sigma} \frac{1}{\Delta f} \mathbf{P}_j dV + \int_{V_e} \mathbf{Q}_i \left(\mathbf{A} c_g(\mathbf{r})^{t,\sigma} + \mathbf{M}\mathbf{u}(\mathbf{r})^{t,\sigma} \right) \cdot \nabla \mathbf{P}_j dV + \int_{V_e} \mathbf{Q}_i \nabla \cdot \left(\mathbf{A} c_g(\mathbf{r})^{t,\sigma} + \mathbf{M}\mathbf{u}(\mathbf{r})^{t,\sigma} \right) \mathbf{P}_j dV \tag{A.3}$$

$$\mathcal{D}_{i,j} = \int_{V_e} \mathbf{Q}_i \mathbf{M} \frac{1}{\Delta t} \mathbf{Q}_j dV + \int_{V_e} \mathbf{Q}_i \mathbf{H}_\theta(\mathbf{r})^{t,\sigma} \mathbf{Q}_j dV + \int_{V_e} \mathbf{Q}_i \mathbf{H}_f(\mathbf{r})^{t,\sigma} \frac{1}{\Delta f} \mathbf{Q}_j dV + \int_{\Gamma^e_{out}} \mathbf{Q}_i \left[\left(\mathbf{A} c_g(\mathbf{r})^{t,\sigma} + \mathbf{M}\mathbf{u}(\mathbf{r})^{t,\sigma} \right) \cdot \mathbf{n} \right] \mathbf{Q}_j d\Gamma - \int_{V_e} \nabla \mathbf{Q}_i \cdot \left(\mathbf{A} c_g(\mathbf{r})^{t,\sigma} + \mathbf{M}\mathbf{u}(\mathbf{r})^{t,\sigma} \right) \mathbf{Q}_j dV \tag{A.4}$$

$$\mathbf{S}_{\Phi_i} = \sum_{j=1}^{\eta_Q} \int_{\mathbf{V}} \mathbf{N}_i \mathbf{S}_j \mathbf{Q}_j \tag{A.5}$$

$$\mathbf{S}_{\Theta_i} = \sum_{j=1}^{\eta_Q} \int_{\mathbf{V}} \mathbf{Q}_i \mathbf{S}_j \mathbf{Q}_j \tag{A.6}$$

where i, j correspond to block matrices of size $K \times K$, i.e. they contain the angular discretised information on each spatial node. The integral $\int_{\Gamma_{out}} d\Gamma$ refers to the outgoing component of the boundary integral $\int_\Gamma d\Gamma$.

References

[1] J.A. Battjes, Shallow water wave modeling, in: M. Isaacson, M. Quick (Eds.), Proceeding of International Symposium Waves – Physical and Numerical Modeling, University of British Columbia, Vancouver, ASCE, 1994, pp. 1–23.
[2] W.J. Pierson, G. Neumann, R.W. James, Practical Methods for Observing and Forecasting Ocean Waves by Means of Wave Spectra and Statistics, H.O. Pub., vol. 603, US Navy Hydrographic Office, 1955.
[3] R. Gelci, H. Cazalé, J. Vassal, Prévision de la houle. La méthode des densités spectroangulaires, Bull. Inf. Comité Océanogr. Etude Côtes 9 (1957) 416–435.
[4] L.H. Holthuijsen, Waves in Oceanic and Coastal Waters, Cambridge University Press, 2007.
[5] SWAMP Group, Ocean Wave Modeling, Plenum Press, 1985.
[6] WAMDI group, The WAM model—a third generation ocean wave prediction model, 18 (1988) 1775–1810.
[7] G.B. Whitham, Linear and Nonlinear Waves, A Wiley–Interscience Publication, Wiley, 1974.
[8] P.A.E.M. Janssen, Progress in ocean wave forecasting, in: Predicting Weather, Climate and Extreme Events, J. Comput. Phys. 227 (7) (2008) 3572–3594.
[9] L. Cavaleri, J.H.G.M. Alves, F. Ardhuin, A. Babanin, M. Banner, K. Belibassakis, M. Benoit, M. Donelan, J. Groeneweg, T.H.C. Herbers, P. Hwang, P.A.E.M. Janssen, T. Janssen, I.V. Lavrenov, R. Magne, J. Monbaliu, M. Onorato, V. Polnikov, D. Resio, W.E. Rogers, A. Sheremet, J. McKee Smith, H.L. Tolman, G. van Vledder, J. Wolf, I. Young, Wave modelling – the state of the art, Prog. Oceanogr. 75 (2007) 603–674.
[10] H.L. Tolman, A third-generation model for wind waves on slowly varying, unsteady, and inhomogeneous depths and currents, J. Phys. Oceanogr. 21 (6) (1991) 782–797.
[11] N. Booij, R.C. Ris, L.H. Holthuijsen, A third-generation wave model for coastal regions: 1. Model description and validation, J. Geophys. Res. 104 (C4) (1999) 7649–7666.
[12] F. Ardhuin, A. Roland, Spectral wave models, coastal and coupled effects, in: P. Bonneton, T. Garlan (Eds.), Coastal Dynamics '13, University of Bordeaux, 2013, pp. 25–38.

[13] A. Roland, F. Ardhuin, On the developments of spectral wave models: numerics and parameterizations for the coastal ocean, Ocean Dyn. 64 (6) (2014) 833–846.
[14] T.W. Hsu, S.H. Ou, J.M. Liau, Hindcasting nearshore wind waves using a FEM code for SWAN, Coast. Eng. 52 (2) (2005) 177–195.
[15] J. Qi, C. Chen, R.C. Beardsley, W. Perrie, G.W. Cowles, Z. Lai, An unstructured-grid finite-volume surface wave model (fvcom-swave): implementation, validations and applications, in: The Sixth International Workshop on Unstructured Mesh Numerical Modelling of Coastal, Shelf and Ocean Flows, Ocean Model. 28 (1–3) (2009) 153–166.
[16] A. Roland, Development of WWM II: spectral wave modelling on unstructured meshes, PhD thesis, Technische Universit Darmstadt, Institute of Hydraulics and Water Resources Engineering, 2008.
[17] M. Zijlema, Computation of wind-wave spectra in coastal waters with SWAN on unstructured grids, Coast. Eng. 57 (3) (2010) 267–277.
[18] S. Popinet, Gerris: a tree-based adaptive solver for the incompressible Euler equations in complex geometries, J. Comput. Phys. 190 (2) (2003) 572–600.
[19] M.D. Piggott, G.J. Gorman, C.C. Pain, P.A. Allison, A.S. Candy, B.T. Martin, M.R. Wells, A new computational framework for multi-scale ocean modelling based on adapting unstructured meshes, Int. J. Numer. Methods Fluids 56 (8) (2008) 1003–1015.
[20] S. Popinet, R.M. Gorman, G.J. Rickard, H.L. Tolman, A quadtree-adaptive spectral wave model, Ocean Model. 34 (1–2) (2010) 36–49.
[21] J.D. Meixner, Discontinuous Galerkin methods for spectral wave/circulation modeling, PhD thesis, The University of Texas at Austin, August 2013.
[22] K.C. Ewans, Observations of the directional spectrum of fetch-limited waves, J. Phys. Oceanogr. 28 (1998) 495–512.
[23] I.R. Young, L.A. Verhagen, M.L. Banner, A note on the bimodal directional spreading of fetch limited wind waves, J. Geophys. Res. 100 (1995) 773–778.
[24] I. Daubechies, Ten Lectures on Wavelets, Society for Industrial and Applied Mathematics, Philadelphia, PA, USA, 1992.
[25] B.J. Lucier, R.A. DeVore, B. Jawerth, Image compression through wavelet transform coding, IEEE Trans. Inf. Theory 38 (1992) 719–746.
[26] A. Averbuch, V.A. Zheludev, A new family of spline-based biorthogonal wavelet transforms and their application to image compression, IEEE Trans. Image Process. 13 (7) (2004) 993–1007.
[27] S.G. Chang, B. Yu, M. Vetterli, Adaptive wavelet thresholding for image denoising and compression, IEEE Trans. Image Process. 9 (9) (2000) 1532–1546.
[28] M. Farge, Wavelet transforms and their applications to turbulence, Annu. Rev. Fluid Mech. 24 (1) (1992) 395–458.
[29] G.W. Wei, D.S. Zhang, S.C. Althorpe, D.J. Kouri, D.K. Hoffman, Wavelet-distributed approximating functional method for solving the Navier–Stokes equation, Comput. Phys. Commun. 115 (1) (1998) 18–24.
[30] X. Zhou, Y. He, Using divergence free wavelets for the numerical solution of the 2-d stationary Navier–Stokes equations, Appl. Math. Comput. 163 (2) (2005) 593–607.
[31] M.A. Alves, P. Cruz, A. Mendes, F.D. Magalhães, F.T. Pinho, P.J. Oliveira, Adaptive multiresolution approach for solution of hyperbolic PDEs, Comput. Methods Appl. Mech. Eng. 191 (2002) 3909–3928.
[32] S.M. Reckinger, O.V. Vasilyev, B. Fox-Kemper, Adaptive wavelet collocation method on the shallow water model, in: Frontiers in Computational Physics Modeling the Earth System, J. Comput. Phys. 271 (2014) 342–359.
[33] S.L. Ho, S.Y. Yang, Wavelet–Galerkin method for solving parabolic equations in finite domains, Finite Elem. Anal. Des. 37 (12) (2001) 1023–1037.
[34] G. Chiavassa, M. Guichaoua, J. Liandrat, Two adaptive wavelet algorithms for non-linear parabolic partial differential equations, Comput. Fluids 31 (4–7) (2002) 467–480.
[35] W. Dahmen, Wavelet methods for PDEs — some recent developments, in: Numerical Analysis 2000. Vol. VII: Partial Differential Equations, J. Comput. Appl. Math. 128 (1–2) (2001) 133–185.
[36] E.E. Lewis, W.F. Miller, Computational Methods of Neutron Transport, 1984.
[37] G.J. Komen, L. Cavaleri, M. Donelan, K. Hasselmann, S. Hasselmann, P.A.E.M. Janssen, Dynamics and Modelling of Ocean Waves, Cambridge University Press, 1994, Cambridge Books Online.
[38] A.G. Buchan, C.C. Pain, M.D. Eaton, R.P. Smedley-Stevenson, A.J.H. Goddard, Linear and quadratic octahedral wavelets on the sphere for angular discretisations of the Boltzmann transport equation, Ann. Nucl. Energy 32 (11) (2005) 1224–1273.
[39] A.G. Buchan, C.C. Pain, M.D. Eaton, R.P. Smedley-Stevenson, A.J.H. Goddard, Self-adaptive spherical wavelets for angular discretisations of the Boltzmann transport equation, Nucl. Sci. Eng. 158 (2008) 244–263.
[40] M.A. Goffin, A.G. Buchan, S. Dargaville, C.C. Pain, P.N. Smith, R.P. Smedley-Stevenson, Goal-based angular adaptivity applied to a wavelet-based discretisation of the neutral particle transport equation, J. Comput. Phys. 281 (2015) 1032–1062.
[41] E. Aboufadel, Discovering Wavelets, Wiley, New York, 1999.
[42] C.K. Chui, An Introduction to Wavelets, Wavelet Analysis and Its Applications, Academic Press, 1992.
[43] H. Elman, D. Silvester, A. Wathen, Finite Elements and Fast Iterative Solvers with Applications in Incompressible Fluid Dynamics, first edition, Oxford University Press, 2005.
[44] B.P. Leonard, A stable and accurate convective modelling procedure based on quadratic upstream interpolation, Comput. Methods Appl. Mech. Eng. 19 (1) (1979) 59–98.
[45] A.G. Buchan, A.S. Candy, S.R. Merton, C.C. Pain, J.I. Hadi, M.D. Eaton, A.J.H. Goddard, R.P. Smedley-Stevenson, G.J. Pearce, The inner element sub-grid scale finite element method for the Boltzmann transport equation, Nucl. Sci. Eng. 164 (2) (2010) 105–121.
[46] S.G. Mallat, Multiresolution approximations and wavelet orthonormal bases of $l2(r)$, Trans. Am. Math. Soc. 315 (1) (1989) 69–87.
[47] A.J. Kuik, G.P. van Vledder, L.H. Holthuijsen, A method for the routine analysis of pitch-and-roll buoy wave data, J. Phys. Oceanogr. 18 (1988) 1020–1034.
[48] N. Booij, L.H. Holthuijsen, Propagation of ocean waves in discrete spectral wave models, J. Comput. Phys. 68 (2) (1987) 307–326.
[49] H.L. Tolman, Alleviating the garden sprinkler effect in wind wave models, Ocean Model. 4 (3–4) (2002) 269–289.